Supporting Information for

Gate-Tuning Hybrid Polaritons in Twisted

α-MoO$_3$/Graphene Heterostructures

Zhou Zhou,[†,‡,△] Renkang Song,[†,△] Junbo Xu,[†,△] Xiang Ni,[¶,§] Zijia Dang,[∥] Zhichen Zhao,[†]

Jiamin Quan,[¶,⊥] Siyu Dong,[†] Weida Hu,[#] Di Huang,[†] Ke Chen,[*,∥] Zhanshan Wang,[†,‡] Xinbin

Cheng,[†,‡] Markus B. Raschke,[*,@] Andrea Alù,[*,¶,⊥] and Tao Jiang[*,†]

†*MOE Key Laboratory of Advanced Micro-Structured Materials, Shanghai Frontiers Science Center of*

Digital Optics, Institute of Precision Optical Engineering, and School of Physics Science and Engineering,

Tongji University, Shanghai 200092, China

‡*Shanghai Institute of Intelligent Science and Technology, Tongji University, Shanghai 200092, China*

¶*Photonics Initiative, Advanced Science Research Center, City University of New York, New York, NY,*

10031, USA

§*School of Physics, Central South University, Changsha, Hunan, 410083, China*

∥*Center for the Physics of Low-Dimensional Materials, School of Physics and Electronics, School of Future*

Technology, Henan University, Kaifeng, 475004, China

⊥*Physics Program, Graduate Center, City University of New York, New York, NY, 10026, USA*

#*State Key Laboratory of Infrared Physics, Shanghai Institute of Technical Physics, Chinese Academy of*

Sciences, Shanghai 200083, China

@*Department of Physics and JILA, University of Colorado, Boulder, CO 80309, USA*

△*Contributed equally to this work*

E-mail: kchen@henu.edu.cn; markus.raschke@colorado.edu; aalu@gc.cuny.edu;

tjiang@tongji.edu.cn

Contents

Section 1. Determination of graphene CNP and E_F

The accurate determination of the CNP in our devices is achieved using two distinct methods, i.e., gate-dependent electronic transport measurements and THG intensity measurements. Specifically, in electric transport measurements, we obtained the graphene resistance curve as a function of back-gate voltage V_g by recording the graphene resistance during the gate-tuning near-field experiment (Figure S1a and c). The peak value of the resistance curve corresponds to the graphene CNP. On the other hand, in THG intensity measurements, we recorded the gate-dependent THG signal while sweeping the V_g (Figure S1b, d, e and f). The THG intensity of graphene will be minimum when V_g is tuned to the CNP.[1] Thus, we can also determine the CNP from the THG intensity curve. The advantages of THG measurement lie in its ability to precisely determine the CNP of monolayer graphene located directly beneath the single-layer or twisted bilayer α-MoO$_3$ where we performed the near-field measurements. This approach allows us to eliminate the influence of inhomogeneous doping in graphene on the V_g value of CNP and accurately evaluate the properties of the graphene region involved in the hybrid polariton system. Noting that during both electric transport and THG measurements, devices were maintained in a dry air environment to avoid the effects of atmospheric moisture on the devices. In general, the CNP obtained from these two independent approaches is in good agreement (Figure S1). The precise determination of CNP provides a solid foundation for systematically studying and understanding the gate-tuning behavior of HPPPs.

Based on the precise acquisition of the CNP for graphene as detailed below, we are able to accurately calculate and determine the E_F. The relationship between E_F and carrier density n in graphene is:

$$E_F = \hbar \left| v_F \right| \sqrt{\pi n} \tag{S1}$$

where v_F is the Fermi velocity in graphene (1.1×10^6 m/s), and $\hbar$ is the reduced Planck's

constant. In our devices, E_F is modulated by the back-gate voltage V_g through:[2]

$$V_g - V_{CNP} = \frac{E_F}{e} + \frac{ne}{C_g} \tag{S2}$$

where V_{CNP} is the voltage at the CNP, e is the electron charge, and $C_g = \varepsilon\varepsilon_0/d_g$ is the gate capacitance with ε_0, ε, and d_g represent the permittivity of vacuum, the dielectric constant and the thickness of the gating material ($285\,\mathrm{nm}$ SiO_2 in our devices), respectively. We can thus derive the E_F from equation (S2).
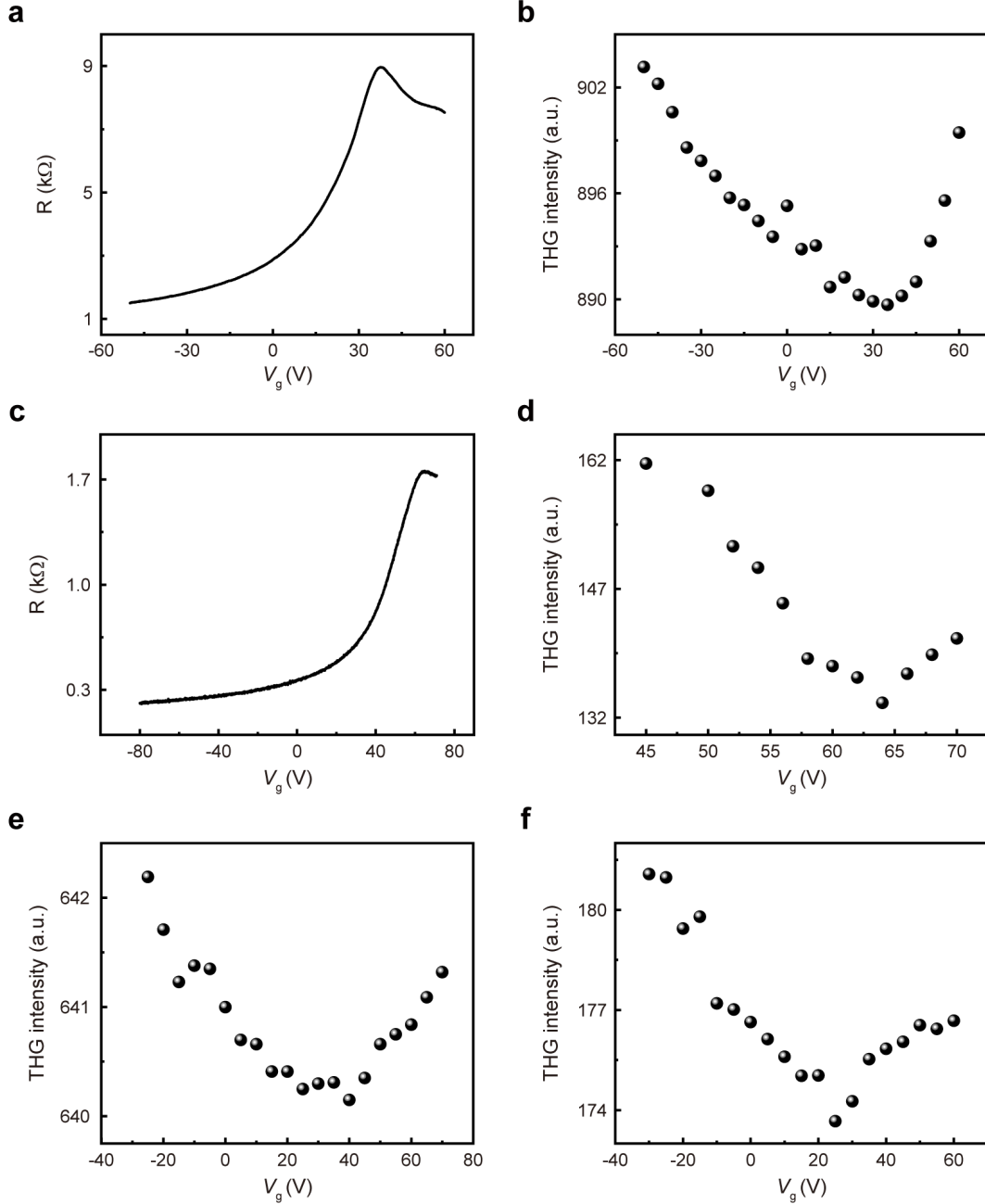
Figure S1. Measured dependence of graphene resistance R and THG intensity on V_g. (a,b) Dependence of (a) graphene resistance and (b) THG intensity on V_g for the 140 nm single-layer α-MoO$_3$/graphene device (Figure 2 in the main text). (c,d) Dependence of (c) graphene resistance and (d) THG intensity on V_g for the twisted bilayer α-MoO$_3$/graphene device (Figure 3b and c in the main text). (e,f) Dependence of THG intensity on V_g for (e) the 175 nm single-layer α-MoO$_3$/graphene device (Figure S14) and (f) the twisted bilayer α-MoO$_3$/graphene device (Figure 3d-i in the main text).

Section 2. Numerical simulations

The real-space full-wave simulations of HPPPs were conducted using the finite-difference time-domain (FDTD) method, employing the commercially available software Lumerical FDTD (2020b, http://www.lumerical.com/tcad-products/fdtd/). A linearly polarized plane-wave was used to acquire HPPP fringes excited by α-MoO$_3$ edges. The real part of the out-of-plane electric field Re (E_z) was monitored.

The conductivity of graphene is given by non-approximate Kubo formula:[3]

$$\sigma(\omega, \tau, E_F, T) = \sigma_{\text{intra}}(\omega, \tau, E_F, T) + \sigma_{\text{inter}}(\omega, \tau, E_F, T) \tag{S3}$$

$\sigma_{\text{intra}}(\omega, \tau, E_F, T)$ and $\sigma_{\text{inter}}(\omega, \tau, E_F, T)$ are the contributions from intraband and interband electron-photon scattering processes, respectively:

$$\sigma_{\text{intra}}(\omega, \tau, E_F, T) = \frac{-ie^2}{\pi\hbar^2(\omega + \frac{i}{\tau})} \int_0^\infty \xi \left(\frac{\partial f_d(\xi)}{\partial \xi} - \frac{\partial f_d(-\xi)}{\partial \xi} \right) d\xi \tag{S4}$$

$$\sigma_{\text{inter}}(\omega, \tau, E_F, T) = \frac{ie^2(\omega + \frac{i}{\tau})}{\pi\hbar^2} \int_0^\infty \frac{f_d(-\xi) - f_d(\xi)}{(\omega + \frac{i}{\tau})^2 - 4(\frac{\xi}{\hbar})^2} d\xi \tag{S5}$$

where τ is phenomenological relaxation time of graphene, E_F is graphene Fermi energy, T is the temperature, $\hbar$ is the reduced Plank constant, $f_d(\xi) \equiv \frac{1}{e^{(\xi - E_F)/(k_B T)} + 1}$ is the Fermi-Dirac distribution, and k_B is Boltzmann constant.

Considering that τ is influenced by various factors such as temperature, sample quality, carrier mobility, and particularly Fermi energy of graphene,[1,4] a fixed value of $\tau = 0.64\,\text{ps}$ is used for simplicity in our work, consistent with previous studies.[5,6] While simulations with a consistent τ capture the primary trend of our experimental data quite well, small deviations can be expected as E_F changes. Nevertheless, we believe this approach is sufficient for offering a comprehensible physical explanation. The calculated real and imaginary parts of $\sigma(E_F)$ are shown in Figure S2a.

6

In the mid-infrared region, the optical response of the α-MoO₃ is dominated by photon absorption instead of electronic transition. The permittivity tensor of α-MoO₃, denoted as $\bar{\bar{\varepsilon}}_{MoO_3}$, can be described using the Lorentz oscillator:

$$\varepsilon_j(\omega) = \varepsilon_j^\infty \left(1 + \frac{\omega_j^{LO^2} - \omega_j^{TO^2}}{\omega_j^{TO^2} - \omega^2 - i\omega\Gamma_j}\right), \ j = x, \ y, \ z \tag{S6}$$

where $\varepsilon_j(\omega)$ is the diagonal component of the $\bar{\bar{\varepsilon}}_{MoO_3}$ at light frequency ω, $\varepsilon_j^\infty = \varepsilon_j(\infty)$, ω_j^{LO} and ω_j^{TO} are the longitude optical (LO) and transverse optical (TO) phonon frequencies, and Γ_j is the damping constant. The value of these parameters are obtained from the literature.[7] The real and imaginary parts of $\varepsilon_j(\omega)$ are shown in Figure S2c and d, respectively. The permittivity of SiO_2 is obtained from the literature.[8]
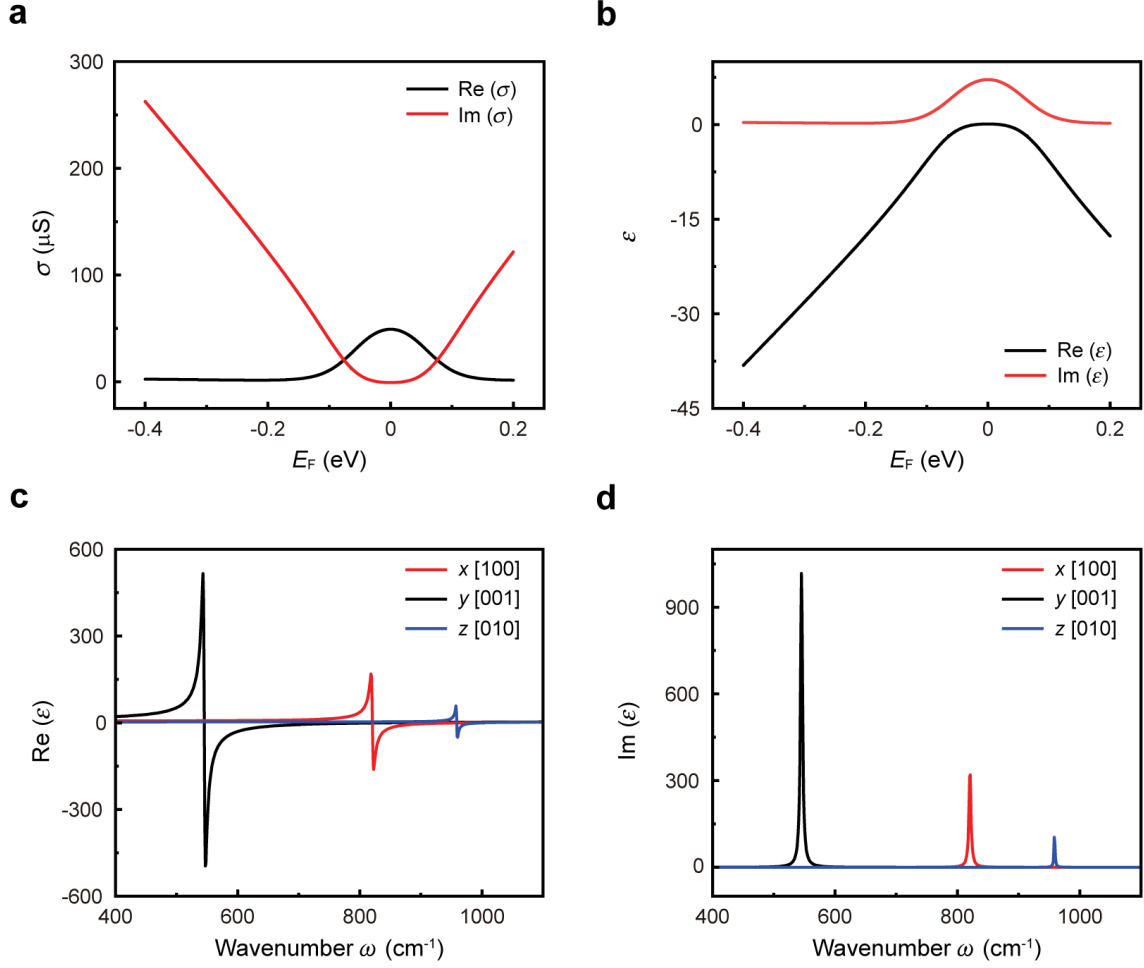
Figure S2. Optical properties of graphene and α-MoO$_3$. (a,b) Dependence of the real (black curve) and imaginary (red curve) parts of (a) graphene conductivity and (b) relative permittivity on E_F at $931\,\text{cm}^{-1}$. (c,d) (c) Real and (d) imaginary parts of α-MoO$_3$ relative permittivity along the x[100] (red curve), y[001] (black curve), and z[010] (blue curve) crystal directions.

Section 3. Calculation of polariton dispersion

Transfer matrix method (TMM) was used to calculate the dispersion relation of HPPPs.[9] In our model, the single-layer α-MoO$_3$/graphene heterostructure was regarded as a structure containing four infinite large layers, i.e., air/α-MoO$_3$/graphene/SiO$_2$ (Figure S3a). Similarly, the twisted bilayer α-MoO$_3$/graphene heterostructure was modeled as a structure containing five infinite large layers, i.e., air/top α-MoO$_3$/bottom α-MoO$_3$/graphene/SiO$_2$ (Figure S3b).

We assumed graphene has a very small thickness Δ with bulk conductivity $\sigma_{g,v} = \sigma_g/\Delta$, where σ_g is graphene conductivity. Thus we can treat graphene as a bulk dielectric material with equivalent complex permittivity $\varepsilon_{g,v} = \frac{\sigma_{g,v}}{-i\omega} + \varepsilon_0$, where ε_0 is the permittivity of vacuum.[10] The imaginary part of the reflection coefficient for p-polarized incident beams r_{pp} was used to visualize the polariton dispersion.
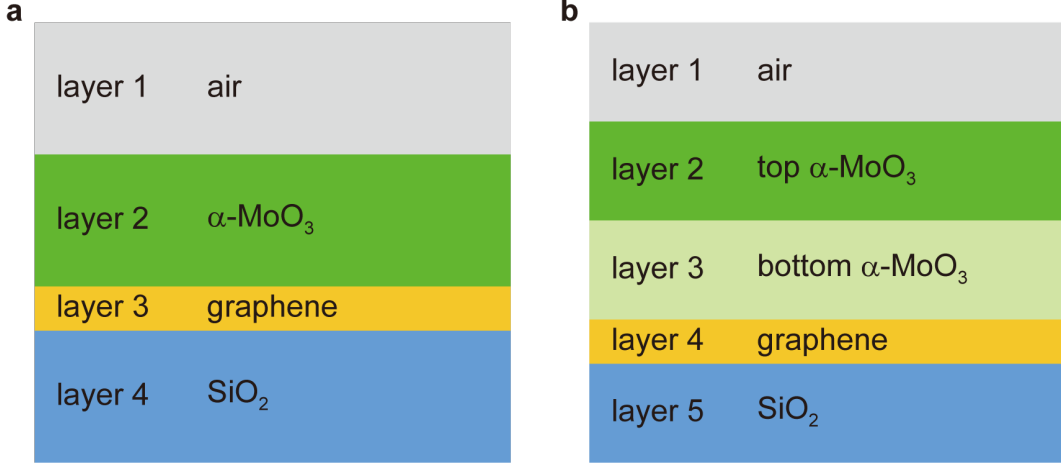

Figure S3. Illustration of the layered structures used in calculating polariton dispersion with transfer matrix method. (a,b) Layered structure of the (a) single-layer and (b) twisted bilayer α-MoO$_3$/graphene. Gray, dark green, light green, yellow, and blue areas represent air, top α-MoO$_3$ layer, bottom α-MoO$_3$ layer, graphene, and SiO$_2$, respectively. The thickness of graphene layer is 0.34 nm.

Section 4. Theoretical calculation of relation between HPPP complex momentum and graphene conductivity

The relationship between the complex momentum of HPPPs and the conductivity of graphene was theoretically calculated using electromagnetic wave theory with appropriate boundary conditions. In the calculation, α-MoO$_3$ and graphene were modeled as two-dimensional infinite conductors. The conductivity tensor of α-MoO$_3$ $\bar{\bar{\sigma}}_{\mathrm{MoO_3}}$ satisfies:

$$\bar{\bar{\sigma}}_{\mathrm{MoO_3}} = -i\omega d_t \varepsilon_0 \bar{\bar{\varepsilon}}_{\mathrm{MoO_3}} \tag{S7}$$

where ω is the frequency of excitation laser, d_t is the thickness of α-MoO$_3$, ε_0 is the permittivity of vacuum, and $\bar{\bar{\varepsilon}}_{\text{MoO}_3}$ is the second-order permittivity tensor of α-MoO$_3$. Due to the significant field confinement in the structure, only transverse magnetic (TM) modes were considered in our theoretical calculation, as the contribution of transverse electric (TE) components was deemed negligible.

For the single-layer α-MoO$_3$/graphene heterostructure, the entire structure was divided into three regions by the α-MoO$_3$ layer at $z = 0$ and the graphene layer at $z = d$ ($d < 0$) : region 1 ($z > 0$, air), region 2 ($d < z < 0$, free space), and region 3 ($z < d$, SiO$_2$ substrate) (Figure S4a). The boundary conditions for electromagnetic waves are:

$$\hat{z} \times (\boldsymbol{E}_1 - \boldsymbol{E}_2) = 0, \ \hat{z} \times (\boldsymbol{H}_1 - \boldsymbol{H}_2) = \bar{\bar{\sigma}}_{\text{MoO}_3}\boldsymbol{E}_{1,\,at\,z=0} \tag{S8}$$

$$\hat{z} \times (\boldsymbol{E}_2 - \boldsymbol{E}_3) = 0, \ \hat{z} \times (\boldsymbol{H}_2 - \boldsymbol{H}_3) = \bar{\bar{\sigma}}_{\text{Gr}}\boldsymbol{E}_{3,\,at\,z=d} \tag{S9}$$

where $\boldsymbol{E}_i$ and $\boldsymbol{H}_i$ are electric and magnetic fields in region i, $i = 1, 2, 3$, respectively, and $\bar{\bar{\sigma}}_{\text{Gr}}$ is the conductivity tensor of graphene. In the xyz coordinate, the general solutions for electromagnetic waves in different regions parallel to the interfaces are:

$$\boldsymbol{H}_1 = \hat{\boldsymbol{y}}A_1^+ e^{iq_{z_1}z} \tag{S10}$$

$$\boldsymbol{E}_1 = \hat{\boldsymbol{x}}A_1^+ \frac{-1}{\omega\varepsilon_1}(-q_{z_1})e^{iq_{z_1}z} \tag{S11}$$

$$\boldsymbol{H}_2 = \hat{\boldsymbol{y}}(A_2^+ e^{+iq_{z_2}z} + A_2^- e^{-iq_{z_2}z}) \tag{S12}$$

$$\boldsymbol{E}_2 = \hat{\boldsymbol{x}}\frac{-1}{\omega\varepsilon_2}(-q_{z_2}A_2^+ e^{+iq_{z_2}z} + q_{z_2}A_2^- e^{-iq_{z_2}z}) \tag{S13}$$

$$\boldsymbol{H}_3 = \hat{\boldsymbol{y}}A_3^- e^{-iq_{z_3}z} \tag{S14}$$

$$\boldsymbol{E}_3 = \hat{\boldsymbol{x}}\frac{-1}{\omega\varepsilon_3}(+q_{z_3}A_3^- e^{-iq_{z_3}z}) \tag{S15}$$

where $q_{z_i} = \sqrt{\frac{\omega^2}{c^2}\varepsilon_{r_i} - (2\pi \cdot q_{\text{p}}^{/\!/})^2}$ is the out-of-plane momentum of HPPPs in region i, $q_{\text{p}}^{/\!/}$ is the in-plane momentum of HPPPs, and $\varepsilon_{r_i} = \varepsilon_i/\varepsilon_0$ is the relative permittivity of region i, $i = 1, 2, 3$. The boundary conditions in equations (S8, S9) combined with general solutions

(S10-15) can be simplified into a matrix form as:

$$T_1 A_1 = 0 \tag{S16}$$

where

$$T_1 = \begin{pmatrix} \frac{q_{z_1}}{\omega\varepsilon_1} & -\frac{q_{z_2}}{\omega\varepsilon_2} & \frac{q_{z_2}}{\omega\varepsilon_2} & 0 \\ -1 - \frac{q_{z_1}\sigma_1}{\omega\varepsilon_1} & 1 & 1 & 0 \\ 0 & \frac{q_{z_2}e^{iq_{z_2}d}}{\omega\varepsilon_2} & -\frac{q_{z_2}e^{-iq_{z_2}d}}{\omega\varepsilon_2} & \frac{q_{z_3}e^{-iq_{z_3}d}}{\omega\varepsilon_3} \\ 0 & -e^{iq_{z_2}d} & -e^{-iq_{z_2}d} & (1 + \frac{q_{z_3}\sigma_2}{\omega\varepsilon_3})e^{-iq_{z_3}d} \end{pmatrix}, A_1 = \begin{pmatrix} A_1^+ \\ A_2^+ \\ A_2^- \\ A_3^- \end{pmatrix},$$

$\sigma_1 = \bar{\bar{\sigma}}_{MoO_3,xx}$, and $\sigma_2 = \bar{\bar{\sigma}}_{Gr,xx}$. In order for equation (S16) to have a non-zero solution, the determinant of T_1 must equal zero. Consequently, we can establish a correlation between the conductivity of graphene and the out-of-plane momentum q_{z_i} of HPPPs in single layer α-MoO$_3$/graphene heterostructure:

$$-(q_{z_2}\sigma_2 - \varepsilon_2\omega)(q_{z_1}q_{z_2}\sigma_1 - \varepsilon_2 q_{z_1}\omega + \varepsilon_1 q_{z_2}\omega) + e^{2id_1 q_{z_2}}(q_{z_2}\sigma_2 + \varepsilon_2\omega)(q_{z_1}q_{z_2}\sigma_1 + \varepsilon_2 q_{z_1}\omega + \varepsilon_1 q_{z_2}\omega) = 0 \tag{S17}$$

To calculate the twisted bilayer α-MoO$_3$/graphene structure (Figure S4b), we positioned the bottom α-MoO$_3$ layer in the xyz coordinate, and rotated the top layer with respect to the bottom with a twist angle δ (i.e., the angle between the [100] crystal directions of the two α-MoO$_3$ layers, as shown in Figure S4c). In order to obtain the conductivity tensor of the top α-MoO$_3$ layer in the xyz coordinate, we defined a rotation matrix U:

$$U = \begin{pmatrix} \cos\delta & -\sin\delta \\ \sin\delta & \cos\delta \end{pmatrix} \tag{S18}$$

In the xyz coordinate, the conductivity tensor of the top α-MoO$_3$ layer $\bar{\bar{\sigma}}'_{MoO_3}$ and the bottom α-MoO$_3$ layer $\bar{\bar{\sigma}}_{MoO_3}$ satisfy:

$$\bar{\bar{\sigma}}'_{MoO_3} = U\bar{\bar{\sigma}}_{MoO_3}U^T \tag{S19}$$

that is

$$\bar{\bar{\sigma}}'_{\text{MoO}_3} = \begin{pmatrix} \sigma_{\text{MoO}_3,\text{xx}}\cos\delta^2 + \sigma_{\text{MoO}_3,\text{yy}}\sin\delta^2 & (\sigma_{\text{MoO}_3,\text{xx}} - \sigma_{\text{MoO}_3,\text{yy}})\cos\delta\sin\delta \\ (\sigma_{\text{MoO}_3,\text{xx}} - \sigma_{\text{MoO}_3,\text{yy}})\cos\delta\sin\delta & \sigma_{\text{MoO}_3,\text{yy}}\cos\delta^2 + \sigma_{\text{MoO}_3,\text{xx}}\sin\delta^2 \end{pmatrix} \tag{S20}$$

Similar to the single-layer α-MoO$_3$ scenario, we can deduce that the determinant of T_2 must satisfy:

$$|T_2| = 0 \tag{S21}$$

where

$$T_2 = \begin{pmatrix} \frac{q_{z_1}}{\omega\varepsilon_1} & -\frac{q_{z_2}}{\omega\varepsilon_2} & \frac{q_{z_2}}{\omega\varepsilon_2} & 0 & 0 & 0 \\ -1-\frac{q_{z_1}\sigma_1}{\omega\varepsilon_1} & 1 & 1 & 0 & 0 & 0 \\ 0 & \frac{q_{z_2}e^{iq_{z_2}d_1}}{\omega\varepsilon_2} & -\frac{q_{z_2}e^{-iq_{z_2}d_1}}{\omega\varepsilon_2} & -\frac{q_{z_3}e^{iq_{z_3}d_1}}{\omega\varepsilon_3} & \frac{q_{z_3}e^{-iq_{z_3}d_1}}{\omega\varepsilon_3} & 0 \\ 0 & (-1-\frac{q_{z_2}\sigma_2}{\omega\varepsilon_2})e^{iq_{z_2}d_1} & (-1+\frac{q_{z_2}\sigma_2}{\omega\varepsilon_2})e^{-iq_{z_2}d_1} & e^{iq_{z_3}d_1} & e^{-iq_{z_3}d_1} & 0 \\ 0 & 0 & 0 & \frac{q_{z_3}e^{iq_{z_3}d_2}}{\omega\varepsilon_3} & -\frac{q_{z_3}e^{-iq_{z_3}d_2}}{\omega\varepsilon_3} & \frac{q_{z_4}e^{-iq_{z_4}d_2}}{\omega\varepsilon_4} \\ 0 & 0 & 0 & -e^{iq_{z_3}d_2} & -e^{-iq_{z_3}d_2} & (1+\frac{q_{z_4}\sigma_3}{\omega\varepsilon_4})e^{-iq_{z_4}d_2} \end{pmatrix},$$

$\sigma_1 = \bar{\bar{\sigma}}'_{\text{MoO}_3,\text{xx}}$, $\sigma_2 = \bar{\bar{\sigma}}_{\text{MoO}_3,\text{xx}}$, and $\sigma_3 = \bar{\bar{\sigma}}_{\text{Gr},\text{xx}}$. From equation (S21), we can establish a correlation between the conductivity of graphene and the out-of-plane momentum q_{z_i} of HPPPs in twisted bilayer α-MoO$_3$/graphene heterostructure.
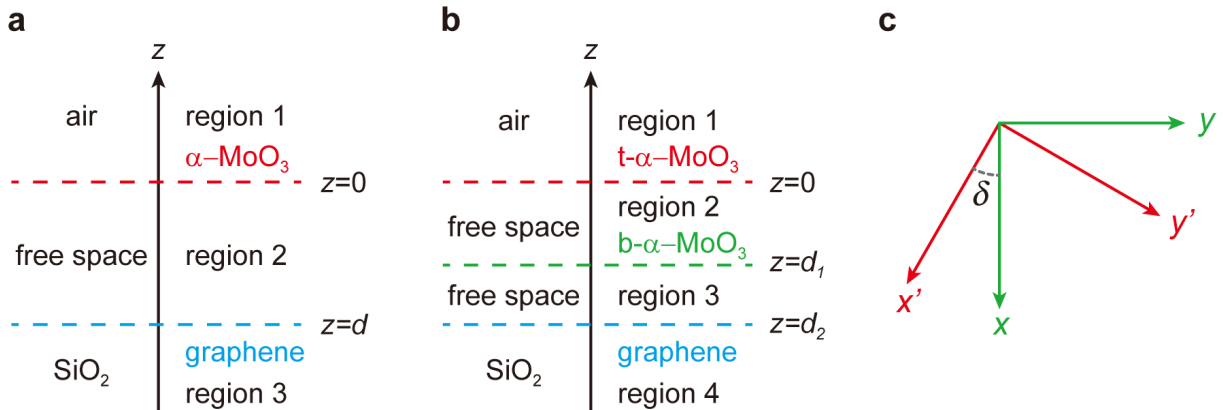
Figure S4. Schematic of the structures used in theoretical calculation with electromagnetic wave theory. (a,b) (a) Single-layer and (b) twisted bilayer α-MoO$_3$/graphene structure. The top and bottom α-MoO$_3$ layers are denoted as t-α-MoO$_3$ and b-α-MoO$_3$, respectively. (c) Coordinates in the xy plane used in the theoretical calculation. δ is the angle between the x' and x axes.

Section 5. Two-phase homodyne near-field detection of the twisted bilayer α-MoO$_3$/graphene device

In homodyne near-field detection scheme where the reference arm is fixed at a specific position (hereinafter, homodyne detection), the amplitude and phase information are convolved in the detected near-field signal.[11] To demonstrate that this convolution does not affect the validity of our experimental findings, we also conducted two phase homodyne detection to extract both the amplitude and phase of near-field images.[12–14] Specifically, we took two measurements where the optical path difference of the reference beam is $\pi/4$ (corresponding to a phase difference of $\pi/2$) and obtained two near-field images, I_{NF_1} and I_{NF_2}. Then we can get the amplitude and phase near-field images by calculating $\sqrt{I_{\mathrm{NF}_1}^2 + I_{\mathrm{NF}_2}^2}$ and arctan($I_{\mathrm{NF}_2}/I_{\mathrm{NF}_1}$), respectively. Figure S5a shows the near-field image of a twisted bilayer α-MoO$_3$/graphene device acquired by homodyne detection with E_{F}=-0.14 eV (corresponding to $V_{\mathrm{g}} = 0$ V). Figure S5b-d show the HPPP λ_{p}, A_{p}, and γ_{p} extracted by fitting line profiles along the [100] crystal direction of the top α-MoO$_3$ layer (white dashed line in Figure

S5a) using different near-field detection schemes. The results demonstrate that despite the convolution of the phase and amplitude in homodyne detection, the gate-tuning behaviors are the same as that obtained from two-phase homodyne amplitude detection. Due to the time-consuming nature of two-phase homodyne detection, particularly in our gate-tuning experiment where we needed to gather two images at each V_g increment, we chose to use homodyne detection to acquire gate-tuning data in other devices.

a E_F = -0.14 eV

b

c

d
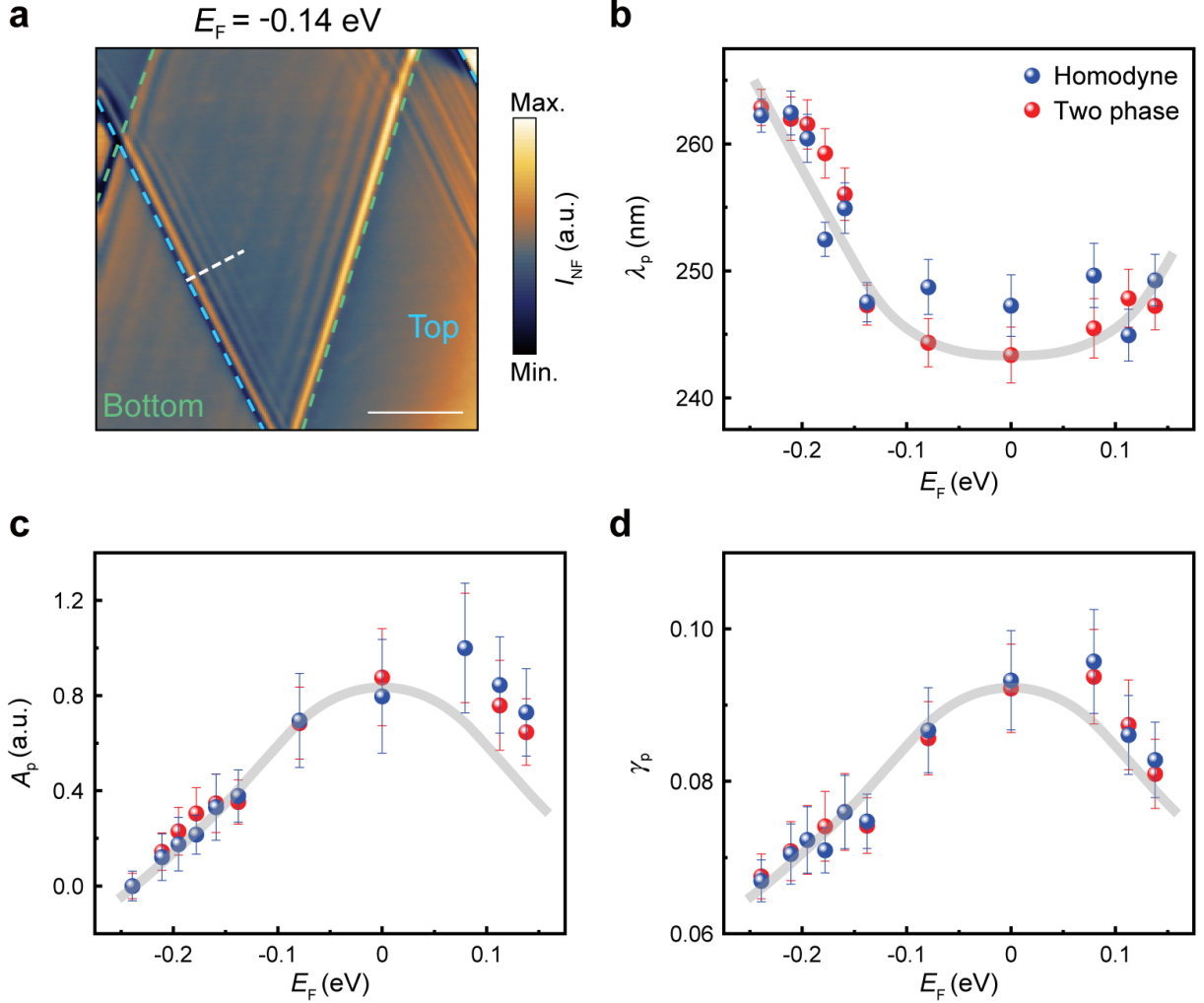
Figure S5. Comparison between homodyne and two-phase homodyne near-field detection. (a) Homodyne near-field image of a twisted bilayer α-MoO$_3$/graphene device with E_F = -0.14 eV (corresponding to $V_g = 0$ V). The thicknesses of the top and bottom α-MoO$_3$ layers are 60 nm and 150 nm, respectively. The twist angle is 47°. The edges of top and bottom α-MoO$_3$ layers are marked by blue and green dashed lines, respectively. Scale bar, 1 μm. (b-d) Dependence of (b) λ_p, (c) normalized A_p, and (d) γ_p on E_F, as fitted from experimental line profiles of HPPPs along the [100] crystal direction of the top α-MoO$_3$ layer (white dashed line in (a)), which are extracted from homodyne (blue dots) and two-phase homodyne amplitude (red dots) near-field images. The error bars represent the 95% confidence intervals. Gray solid lines are guides for the eye.

15

Section 6. Derivation of fitting equations

HPPP wave launches by the tip, which has not spread yet, can be described by the following wave function:

$$\psi_{\text{tip}} = A \tag{S22}$$

where A is the amplitude of the HPPP wave. The HPPP wave propagates along the [100] crystal direction of α-MoO$_3$ and is reflected by the α-MoO$_3$ edge, reaching the tip and interfere with the wave ψ_{tip}. Taking into account the geometric spread, the reflected wave can be expressed as:

$$\psi_{\text{ref}} = ATe^{-iq_{\text{p}}^{/\!/}x}e^{i\phi_0}\frac{1}{\sqrt{x}} \tag{S23}$$

where T is the reflectance of the HPPP wave at the edge, $q_{\text{p}}^{/\!/} = \frac{2\pi}{\lambda_{\text{p}}} + i\frac{2\pi\gamma_{\text{p}}}{\lambda_{\text{p}}}$ is the complex in-plane momentum of the HPPP wave with wavelength λ_{p} and dissipation rate γ_{p}, $e^{i\phi_0}$ is the phase changing after wave reflection, and x is the distance over which the HPPP wave is travelling. The interference between ψ_{tip} and ψ_{ref} gives rise to interference wave ψ_{inter}:

$$\psi_{\text{inter}} = \psi_{\text{tip}} + \psi_{\text{ref}} \tag{S24}$$

Then, the intensity of the interference wave, which is also the intensity of near-field images we measure in the experiment can be expressed by:

$$I_{\text{NF}} = \psi_{\text{inter}} \cdot \psi_{\text{inter}}^* \tag{S25}$$

where ψ_{inter}^* is the complex conjugate of ψ_{inter}. By substituting the equations (S22-24) into (S25), we can deduce the equation used to fit the intensity of IR sSNOM line profiles:

$$I_{\text{NF}} = A_{\text{p}} \cdot \frac{e^{-\frac{2\pi\gamma_{\text{p}}}{\lambda_{\text{p}}}x}}{\sqrt{x}} \cdot \sin(2\pi\frac{x-x_{\text{c}}}{\lambda_{\text{p}}}) + B \cdot \frac{e^{-\frac{4\pi\gamma_{\text{p}}}{\lambda_{\text{p}}}x}}{x} + I_0,\ A_{\text{p}} > 0,\ \gamma_{\text{p}} > 0,\ \lambda_{\text{p}} > 0,\ B > 0 \tag{S26}$$

where $A_p = 2A^2T$, $B = A^2T^2$, and $I_0 = A^2$. A_p, γ_p, λ_p, x_c, B, and I_0 are fitting parameters.

For fitting the simulated HPPP wave, we use a simple damped sine wave function:

$$y = A_p \cdot e^{-\frac{4\pi\gamma_p}{\lambda_p}x} \cdot \sin(2\pi\frac{x - x_c}{\lambda_p}) + y_0, \; A_p > 0, \; \gamma_p > 0, \; \lambda_p > 0 \tag{S27}$$

where A_p, γ_p, λ_p, x_c, and y_0 are fitting parameters. Note that the geometric spread is not considered in equation (S27) since the simulated HPPP waves are excited by a plane-wave.
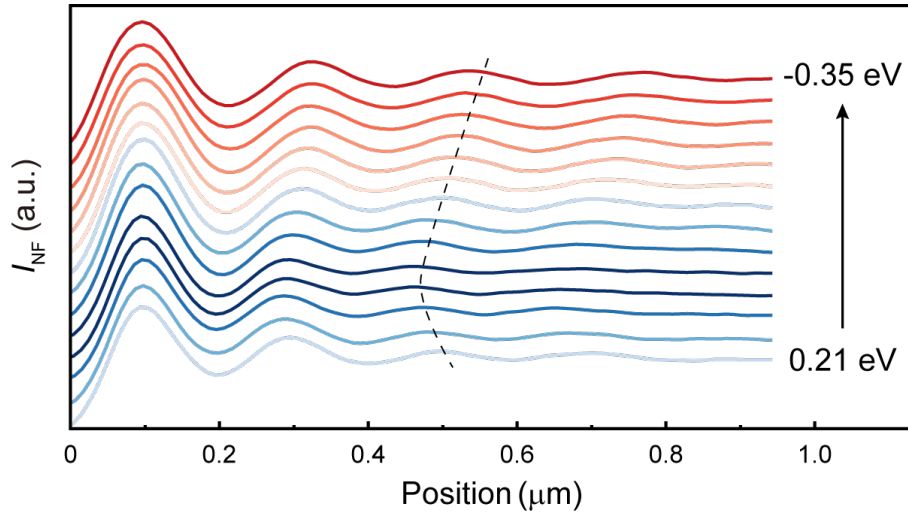
Figure S6. Polariton line profiles of the 140 nm single layer α-MoO$_3$/graphene device. Line profiles extracted along the [100] crystal direction (white dashed line in Figure 2a in the main text) and averaged over 500 nm at different locations in the [001] crystal direction. The back gate voltage V_g was swept from 65 V (corresponding to 0.21 eV, bottom line profile) to -65 V (corresponding to -0.35 eV, top line profile) in increments of 10 V. The black dashed curve indicates the variation trend of λ_p with E_F.

Section 7. Gate-tuning behavior of HPPPs in twisted bilayer α-MoO$_3$/graphene across varying twist angles and α-MoO$_3$ thicknesses

Although our measurements predominantly centered around the twisted bilayer α-MoO$_3$/graphene device with a 47° twist angle, our findings concerning on the gate-tuning behavior of λ_p, A_p, and γ_p remain applicable across all twist angles. To substantiate this claim, we conducted numerical simulations on twisted bilayer α-MoO$_3$/graphene devices, altering the twist angles while maintaining the consistent thicknesses for the top and bottom α-MoO$_3$ layers as presented in Figure 3 in the main text. The results are depicted in Figures S7 and S8. Notably, irrespective of the twist angles considered, the dependency variations of the three parameters on E_F align well with the results and mechanisms elucidated in Figure 3 and Figure 4 in the main text, respectively.

In addition to twist angle, the thickness of α-MoO$_3$ is another factor that can influence the momentum of HPPPs. Our experimental findings, as depicted in Figure 2 and Figure S14, showcase varied thickness of α-MoO$_3$ in the single-layer α-MoO$_3$/graphene device. Moreover, the devices featuring different thicknesses of the top and bottom α-MoO$_3$ layers in the twisted bilayer configuration are presented in Figure 3 and Figure S5. A consistent trend emerges from these data, reinforcing our assertion that the thickness of α-MoO$_3$ does not impact our primary findings on the gate-tuning behaviors of the three key parameters of HPPPs. To further validity this, we performed numerical simulations on a twisted bilayer α-MoO$_3$/graphene device, altering the thicknesses of the top and bottom α-MoO$_3$ layers. The gate-dependent variations of the three HPPP parameters, as detailed in Figure S9 shows the same changing tendency observed in our other twisted devices. The results from our simulations reinforce our conclusions about the gate-tuning behavior of HPPPs in both single-layer and twisted bilayer α-MoO$_3$/graphene heterostructures.
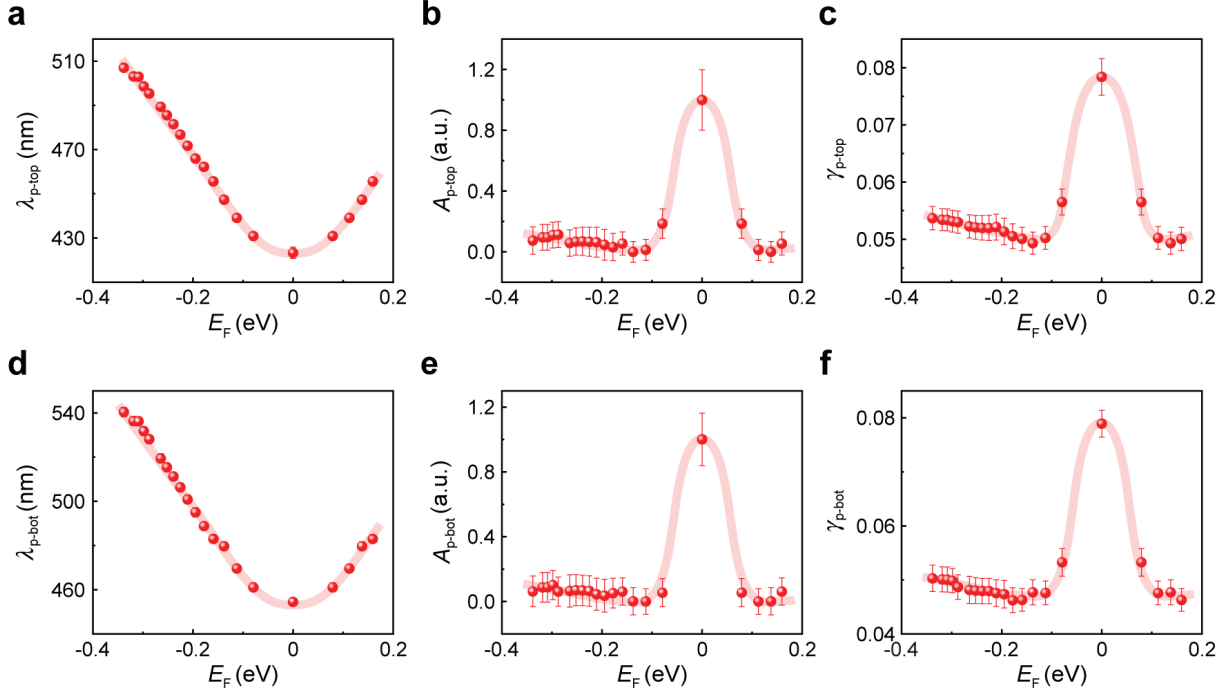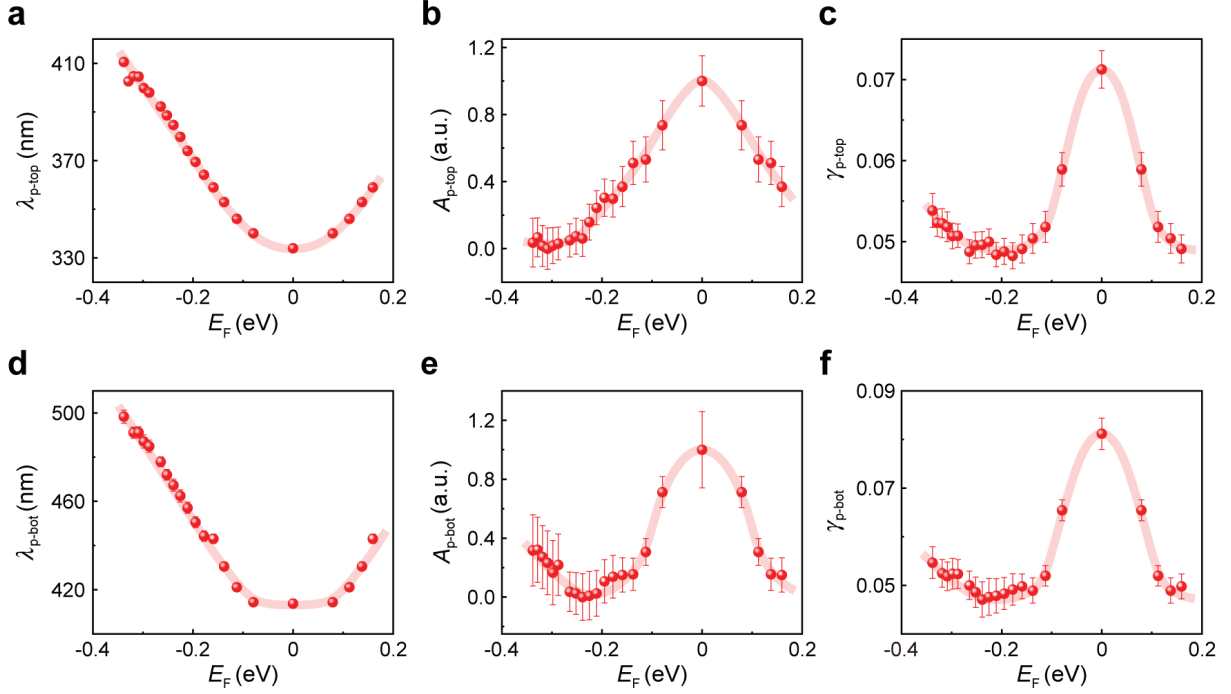
Figure S7. Numerical simulations of gate-tuning behavior of HPPPs in a 20° twisted bilayer α-MoO₃/graphene heterostructure. (a-c) E_F-dependent variations in the (a) wavelength, (b) amplitude, and (c) dissipation rate of HPPPs, extracted from the fitting of simulated HPPP line profiles along the [100] crystal direction of the top α-MoO₃ layer. (d-f) Corresponding variations for the bottom α-MoO₃ layer. The α-MoO₃ layers have thicknesses of 46 nm (top) and 134 nm (bottom). The frequency of incident light is 931 cm^{-1}. The error bars represent the 95% confidence intervals. Red solid lines are guides for the eye.
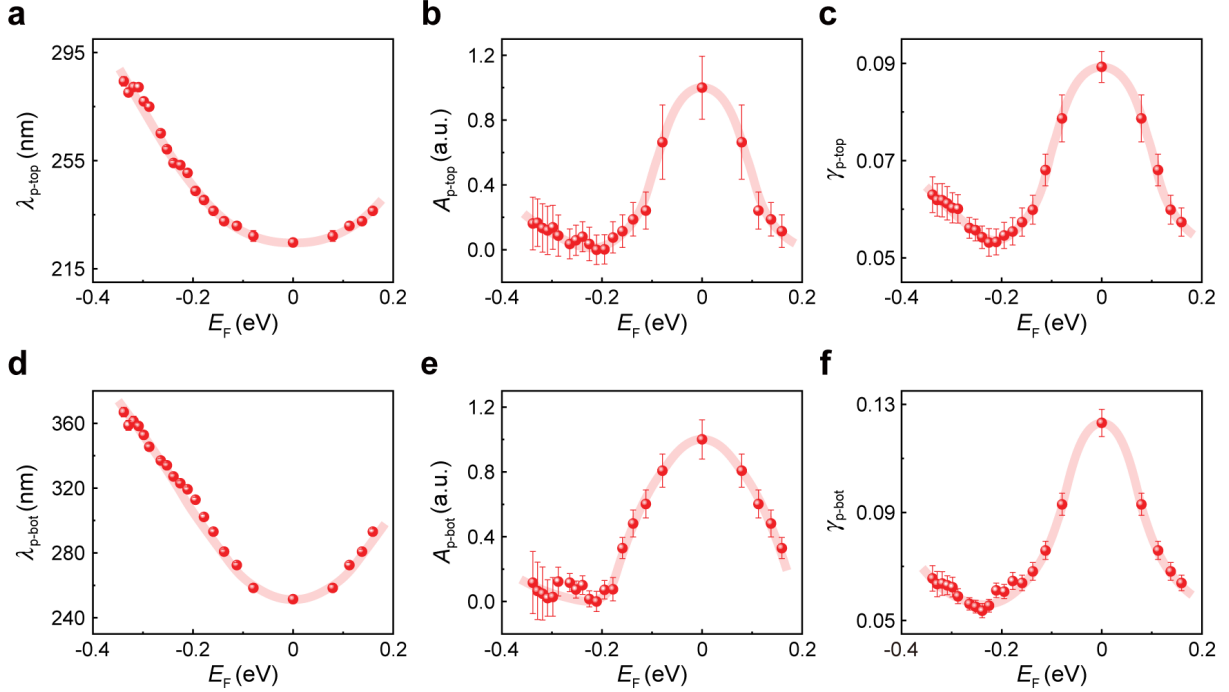
Figure S8. Numerical simulations of gate-tuning behavior of HPPPs in a 35° twisted bilayer α-MoO₃/graphene heterostructure. (a-c) E_F-dependent variations in the (a) wavelength, (b) amplitude, and (c) dissipation rate of HPPPs, extracted from the fitting of simulated HPPP line profiles along the [100] crystal direction of the top α-MoO₃ layer. (d-f) Corresponding variations for the bottom α-MoO₃ layer. The α-MoO₃ layers have thicknesses of 46 nm (top) and 134 nm (bottom). The frequency of incident light is $931\,\text{cm}^{-1}$. The error bars represent the 95% confidence intervals. Red solid lines are guides for the eye.

Figure S9. Numerical simulations of gate-tuning behavior of HPPPs in a 47° twisted bilayer α-MoO$_3$/graphene heterostructure. (a-c) E_F-dependent variations in the (a) wavelength, (b) amplitude, and (c) dissipation rate of HPPPs, extracted from the fitting of simulated HPPP line profiles along the [100] crystal direction of the top α-MoO$_3$ layer. (d-f) Corresponding variations for the bottom α-MoO$_3$ layer. The α-MoO$_3$ layers have thicknesses of 46 nm (top) and 100 nm (bottom). The frequency of incident light is 931 cm^{-1}. The error bars represent the 95% confidence intervals. Red solid lines are guides for the eye.

Section 8. Gate-tuning of topological transition in twisted bilayer α-MoO$_3$/graphene heterostructure

The topological transition of HPPP iso-frequency contours (IFCs), transitioning from an open hyperbolic to a closed elliptical shape, can be influenced by modulating the graphene E_F.[5,15–17] In this section, we elucidate the gate-tuning of this topological transition in a twisted bilayer α-MoO$_3$/graphene heterostructure, utilizing numerical simulations for demonstration. The twist angle for the bilayer α-MoO$_3$ was set to 60°, aligning closely with the photonic magic angle inherent to the heterostructure. The thicknesses of the top and bot-

21

tom α-MoO$_3$ layers were maintained the same as those of the devices showcased in Figure 3 in the main text. The IFCs derived from the FFT analysis of simulated field distributions (specifically, the real component of the z-oriented electric field, Re (E_z)), for E_F values spanning from 0 to -0.7 eV, are presented in Figure S10. Notably, the topological transition occurs at around E_F=-0.4 eV. This gate-tunable topological transition in twisted bilayer α-MoO$_3$/graphene heterostructure showcases the practical application potential of our device configurations.
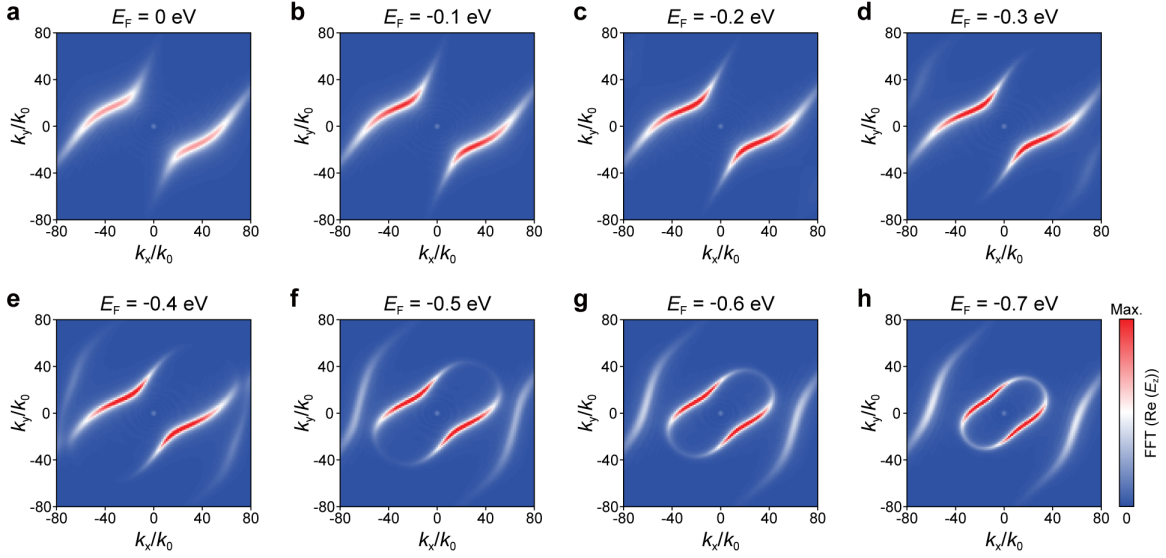
Figure S10. Gate-dependent topological transition in a twisted bilayer α-MoO$_3$/graphene heterostructure with a 60° twist angle. (a-f) Simulated IFCs of twisted bilayer α-MoO$_3$/graphene heterostructure. The graphene E_F varies from 0 to -0.7 eV. The thicknesses of the top and bottom α-MoO$_3$ layers are 46 and 134 nm, respectively. The frequency of incident light is 931 cm^{-1}.
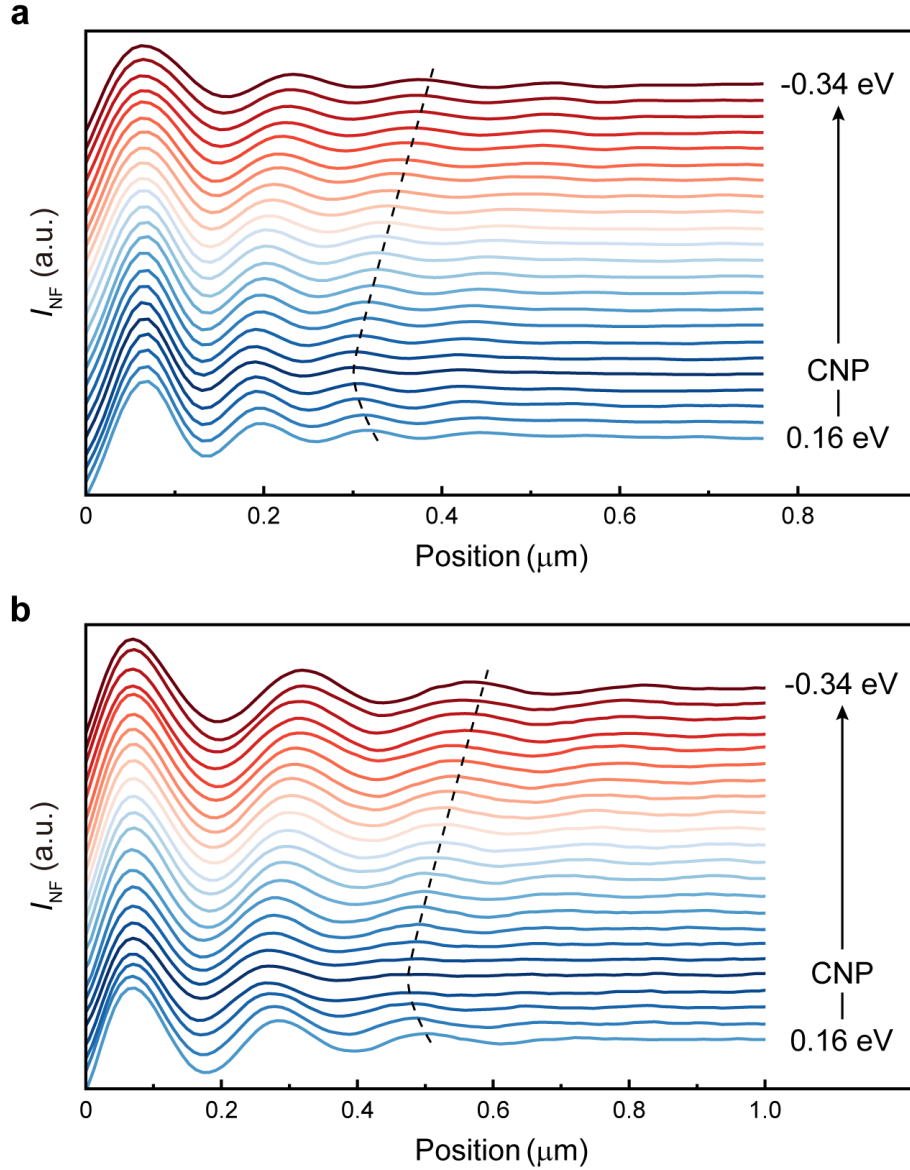
a

b

Figure S11. Polariton line profiles of the twisted bilayer α-MoO$_3$/graphene device. (a,b) Line profiles extracted along the [100] crystal direction of the (a) top (cyan dashed line in Figure 3a in the main text) and (b) bottom (white dashed line in Figure 3a in the main text) layer α-MoO$_3$ and averaged over 500 nm at different locations in the [001] crystal direction. The back gate voltage V_g was swept from 50 V (corresponding to 0.16 eV, bottom line profiles) to -60 V (corresponding to -0.34 eV, top line profiles) in increments of 5 V. The graphene CNP occurs at 30 V. The black dashed curve indicates the variation trend of λ_p with E_F.
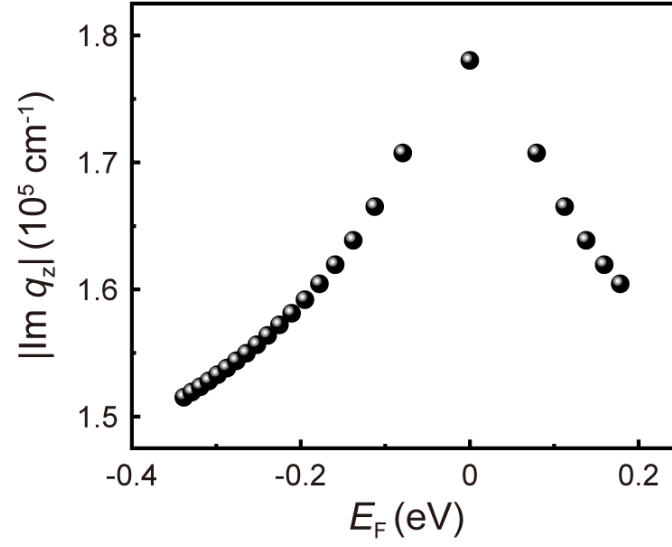
Figure S12. E_F dependence of theoretically calculated absolute value of the imaginary part of HPPP out-of-plane momentum $|\text{Im } q_z|$ along the [100] crystal direction of the bottom α-MoO$_3$ layer .
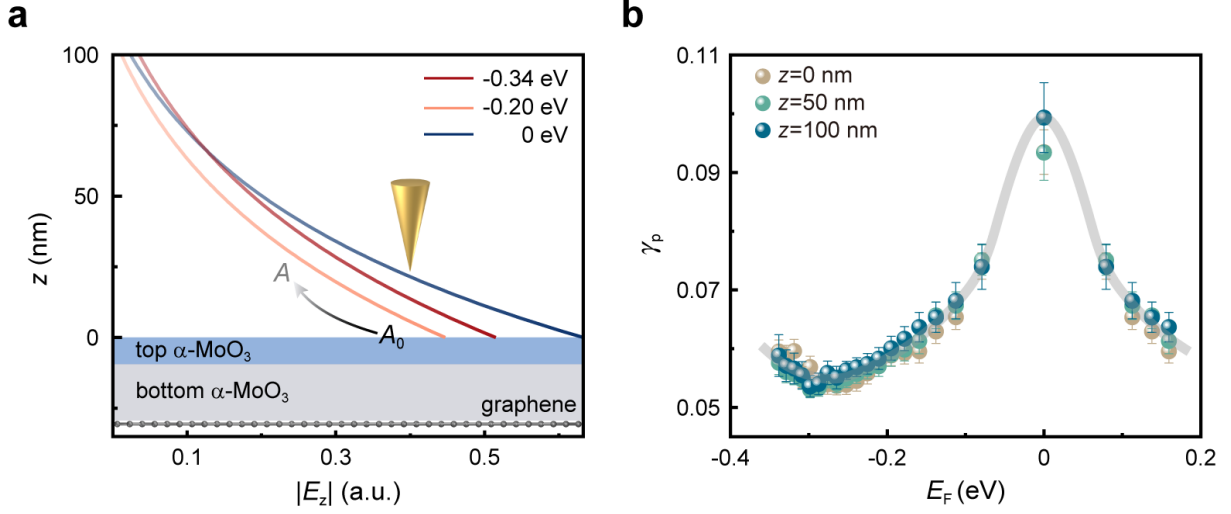
Figure S13. Dependence of electric field distribution and simulated γ_p of HPPPs at different height on E_F. (a) Schematic of the electric field distribution $|E_z|$ of HPPPs in the twisted bilayer α-MoO$_3$/graphene heterostructure along the z direction, with E_F = 0, -0.20 and -0.34 eV. The $|E_z|$ at the surface of the top α-MoO$_3$ layer (z = 0 nm) is denoted by A_0 and decays exponentially to A_p with increasing height z, from which we extract the simulation results. (b) Dependence of simulated γ_p on E_F at different heights (z = 0, 50 and 70 nm) above the surface of the twisted bilayer α-MoO$_3$/graphene, demonstrating independence of z. In both (a) and (b), the direction of $q_p^{\parallel}$ aligns with the [100] crystal direction of the bottom α-MoO$_3$ layer. The error bars represent the 95% confidence intervals. Gray solid line is a guide for the eye.
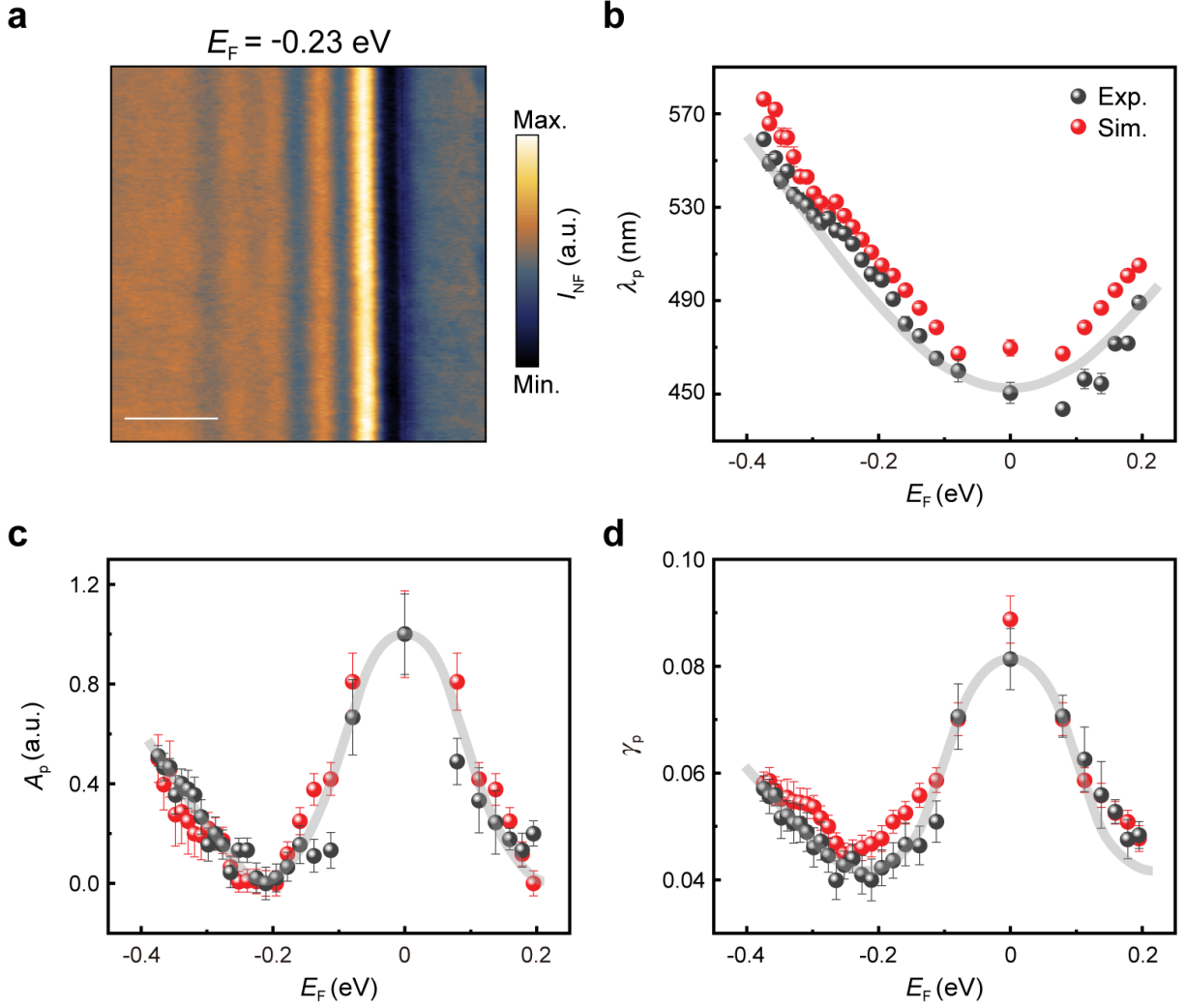
a

E_F = -0.23 eV

b

c

d

Figure S14. Gate-tuning behavior of HPPPs in the 175 nm single-layer α-MoO$_3$/graphene device. (a) Near-field image with $E_F = -0.23$ eV (corresponds to $V_g = 0$ V). Scale bar, 500 nm. (b-d) Dependence of (b) λ_p, (c) normalized A_p, and (d) γ_p on E_F, as fitted from experimental (black dots) and numerically simulated (red dots) line profiles of HPPPs. The error bars represent the 95% confidence intervals. Gray solid lines are guides for the eye.
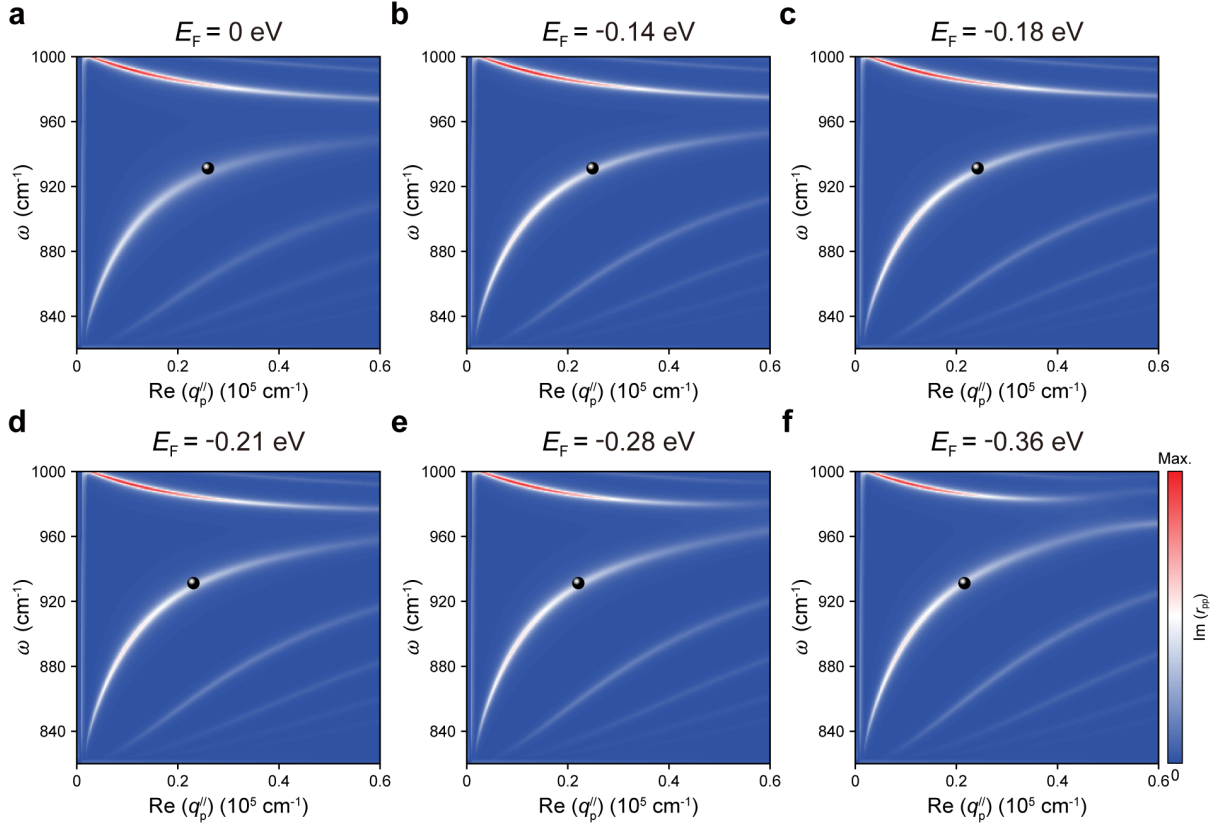
Figure S15. Calculated dispersion of the 140 nm single-layer α-MoO$_3$/graphene heterostructure at various E_F values. Black dots represent experimental data extracted from Figure 2c in the main text.
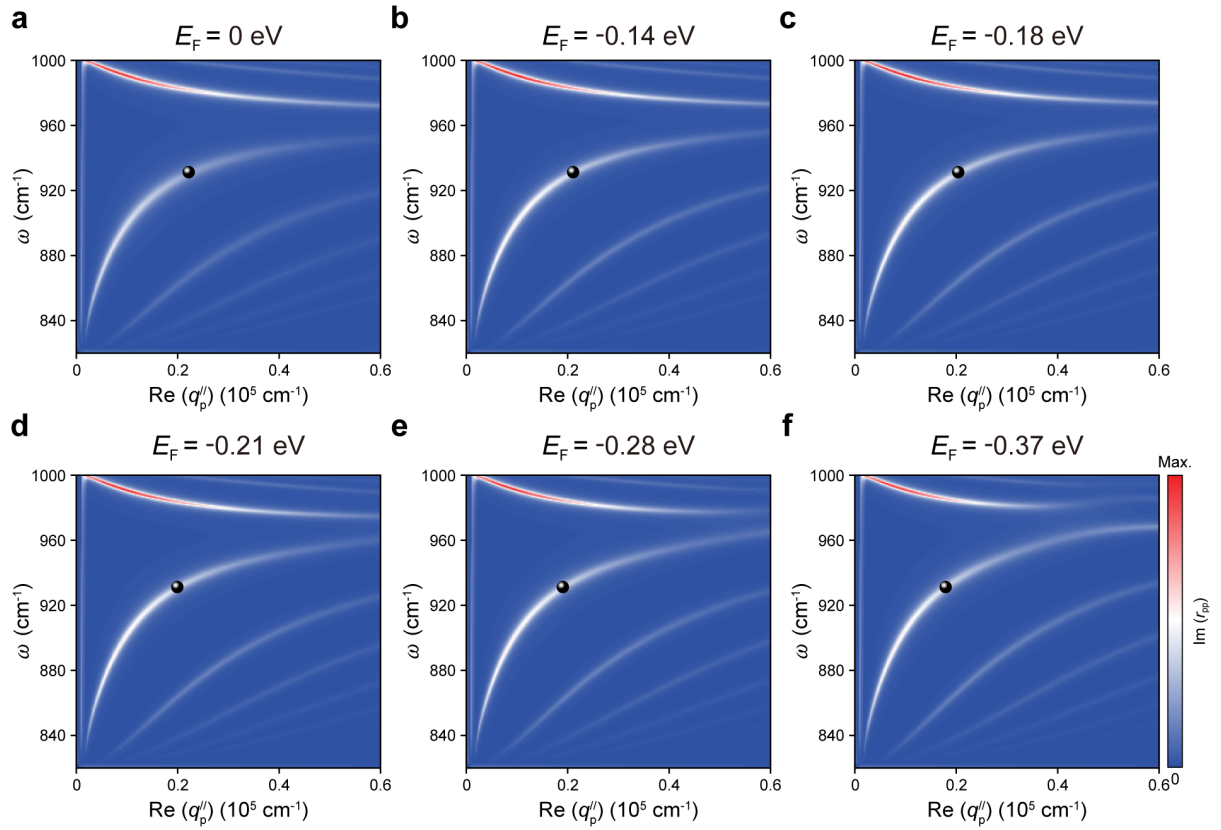
Figure S16. Calculated dispersion of the 175 nm single-layer α-MoO$_3$/graphene heterostructure at various E_F values. Black dots represent experimental data extracted from Figure S14b.
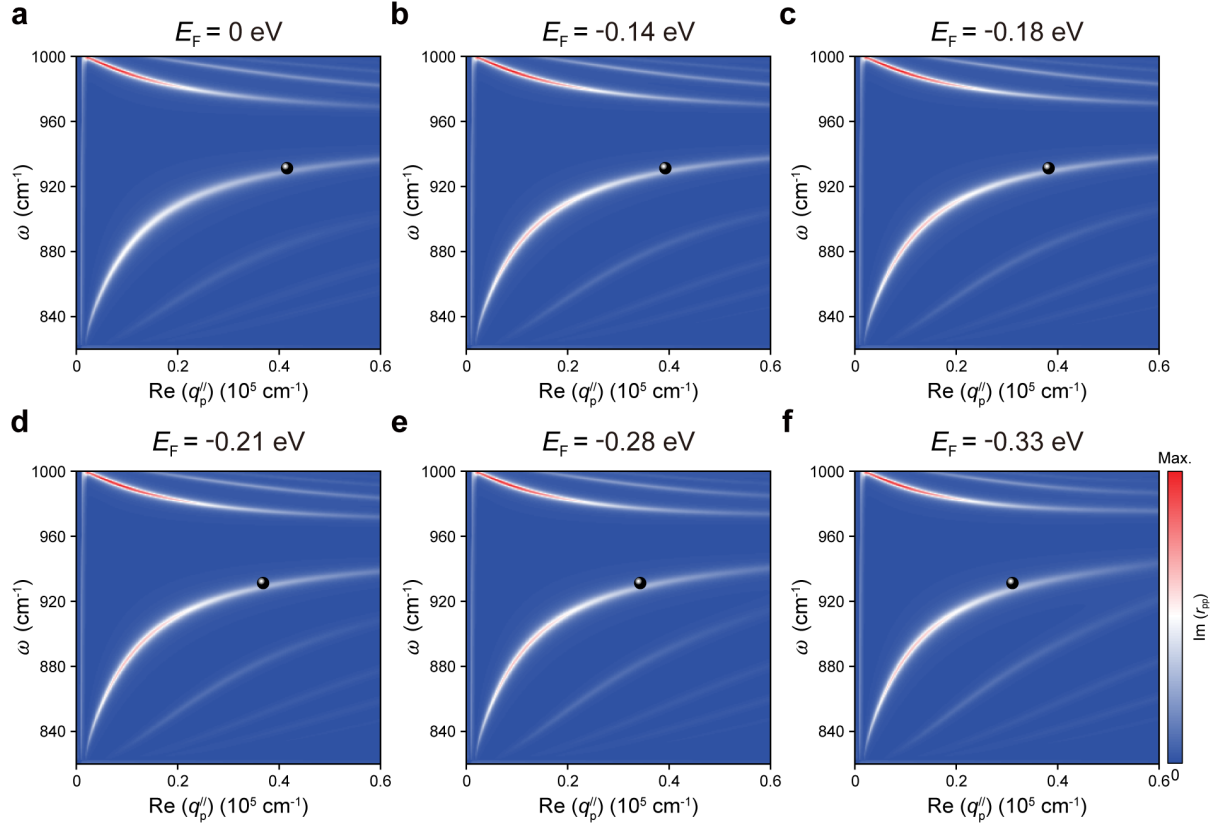
Figure S17. Calculated dispersion of the twisted bilayer α-MoO$_3$/graphene with $q_p^{/\!/}$ along the [100] crystal direction of the top α-MoO$_3$ layer at various E_F values. The α-MoO$_3$ layers in the calculation have the same thickness combination and twisted angle as the device shown in Figure 3 in the main text. Black dots represent experimental data extracted from Figure 3d in the main text.

Figure S18. Calculated dispersion of twisted bilayer α-MoO$_3$/graphene with $q_{\mathrm{p}}^{\!/\!/}$ along the [100] crystal direction of the bottom α-MoO$_3$ layer at various E_{F} values. The α-MoO$_3$ layers in the calculation have the same thickness combination and twisted angle as the device shown in Figure 3 in the main text. Black dots represent experimental data extracted from Figure 3g in the main text.
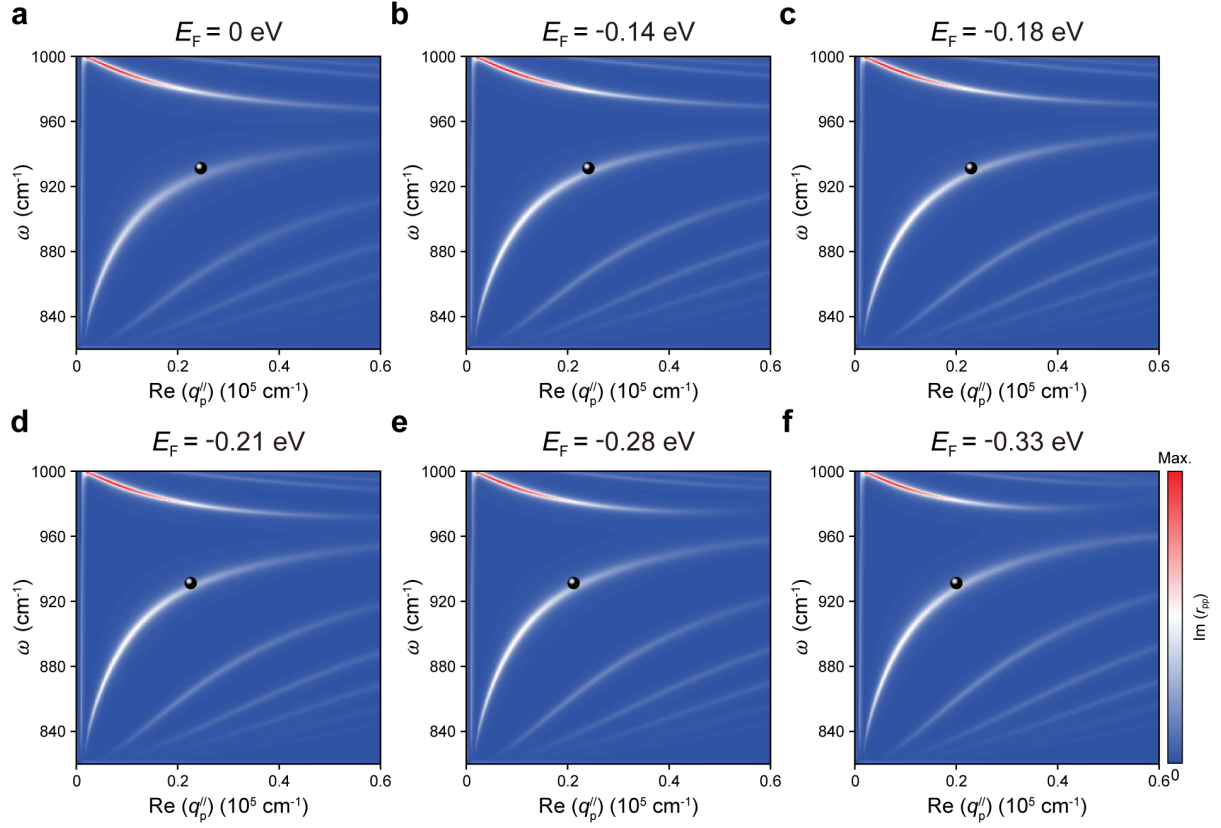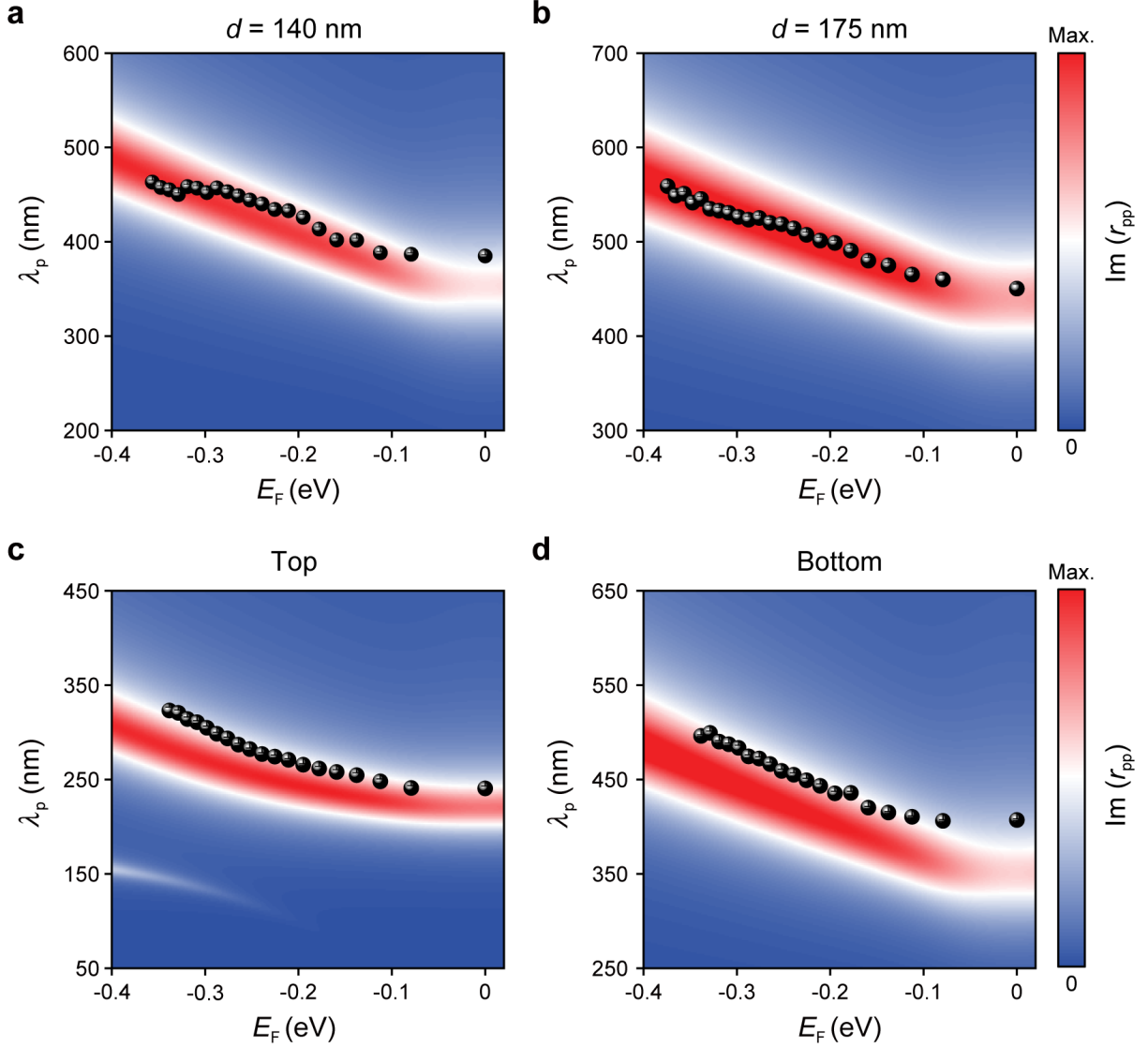
Figure S19. Experimental (black dots) and transfer matrix method calculated (color plots) dependence of λ_p on E_F. (a,b) Single-layer α-MoO$_3$/graphene heterostructures with α-MoO$_3$ thicknesses (a) $d = 140\,\mathrm{nm}$ and (b) $d = 175\,\mathrm{nm}$. (c,d) Twisted bilayer α-MoO$_3$/graphene heterostructures with $q_\mathrm{p}^{/\!/}$ along the [100] crystal direction of the (c) top and (d) bottom α-MoO$_3$ layers. Black dots in (a-d) represent experimental data extracted from Figure 2c, Figure S14b, Figure 3d, and Figure 3g, respectively.

References

(1) Jiang, T. et al. Gate-tunable third-order nonlinear optical response of massless Dirac fermions in graphene. *Nature Photonics* **2018**, *12*, 430–436.

(2) Das, A.; Pisana, S.; Chakraborty, B.; Piscanec, S.; Saha, S. K.; Waghmare, U. V.; Novoselov, K. S.; Krishnamurthy, H. R.; Geim, A. K.; Ferrari, A. C.; Sood, A. K. Monitoring dopants by Raman scattering in an electrochemically top-gated graphene transistor. *Nature Nanotechnology* **2008**, *3*, 210–215.

(3) Falkovsky, L. A. Optical properties of graphene. *Journal of Physics: Conference Series* **2008**, *129*, 012004.

(4) Cheng, J. L.; Vermeulen, N.; Sipe, J. E. Third-order nonlinearity of graphene: Effects of phenomenological relaxation and finite temperature. *Phys. Rev. B* **2015**, *91*, 235320.

(5) Zeng, Y.; Ou, Q.; Liu, L.; Zheng, C.; Wang, Z.; Gong, Y.; Liang, X.; Zhang, Y.; Hu, G.; Yang, Z.; Qiu, C.-W.; Bao, Q.; Chen, H.; Dai, Z. Tailoring Topological Transitions of Anisotropic Polaritons by Interface Engineering in Biaxial Crystals. *Nano Letters* **2022**, *22*, 4260–4268.

(6) Tang, L.; Du, J.; Du, C.; Zhu, P.; Shi, H. Scaling phenomenon of graphene surface plasmon modes in grating-spacer-graphene hybrid systems. *Opt. Express* **2014**, *22*, 20214–20222.

(7) Chen, M.; Lin, X.; Dinh, T. H.; Zheng, Z.; Shen, J.; Ma, Q.; Chen, H.; Jarillo-Herrero, P.; Dai, S. Configurable phonon polaritons in twisted α-MoO$_3$. *Nature Materials* **2020**, *19*, 1307–1311.

(8) Palik, E. D. *Handbook of optical constants of solids*; Academic press, 1998; Vol. 3.

(9) Rumpf, R. C. Improved formulation of scattering matrices for semi-analytical methods

that is consistent with convention. *Progress In Electromagnetics Research B* **2011**, *35*, 241–261.

(10) He, S.; Zhang, X.; He, Y. Graphene nano-ribbon waveguides of record-small mode area and ultra-high effective refractive indices for future VLSI. *Optics Express* **2013**, *21*, 30664–30673.

(11) Gomez, L.; Bachelot, R.; Bouhelier, A.; Wiederrecht, G. P.; Chang, S.-h.; Gray, S. K.; Hua, F.; Jeon, S.; Rogers, J. A.; Castro, M. E.; Blaize, S.; Stefanon, I.; Lerondel, G.; Royer, P. Apertureless scanning near-field optical microscopy: a comparison between homodyne and heterodyne approaches. *Journal of the Optical Society of America B* **2006**, *23*, 823–833.

(12) Taubner, T.; Hillenbrand, R.; Keilmann, F. Performance of visible and mid-infrared scattering-type near-field optical microscopes. *Journal of Microscopy* **2003**, *210*, 311–314.

(13) Taubner, T.; Keilmann, F.; Hillenbrand, R. Nanomechanical Resonance Tuning and Phase Effects in Optical Near-Field Interaction. *Nano Letters* **2004**, *4*, 1669–1672.

(14) Berweger, S.; Nguyen, D. M.; Muller, E. A.; Bechtel, H. A.; Perkins, T. T.; Raschke, M. B. Nano-Chemical Infrared Imaging of Membrane Proteins in Lipid Bilayers. *Journal of the American Chemical Society* **2013**, *135*, 18292–18295.

(15) Hu, H.; Chen, N.; Teng, H.; Yu, R.; Xue, M.; Chen, K.; Xiao, Y.; Qu, Y.; Hu, D.; Chen, J.; Sun, Z.; Li, P.; de Abajo, F. J. G.; Dai, Q. Gate-tunable negative refraction of mid-infrared polaritons. *Science* **2023**, *379*, 558–561.

(16) Hu, H. et al. Doping-driven topological polaritons in graphene/α-MoO_3 heterostructures. *Nature Nanotechnology* **2022**, *17*, 940–946.

(17) Álvarez Pérez, G.; González-Morán, A.; Capote-Robayna, N.; Voronin, K. V.; Duan, J.; Volkov, V. S.; Alonso-González, P.; Nikitin, A. Y. Active Tuning of Highly Anisotropic Phonon Polaritons in Van der Waals Crystal Slabs by Gated Graphene. *ACS Photonics* **2022**, *9*, 383–390.